



The one-pot synthesis, characterisation and catalytic behaviour of mesoporous silica-sulfated zirconia solids

Antony J. Ward, Ajit A. Pujari, Lorenzo Costanzo, Anthony F. Masters, Thomas Maschmeyer*

Laboratory of Advanced Catalysis for Sustainability, School of Chemistry, University of Sydney, NSW 2006, Australia

ARTICLE INFO

Article history:

Received 24 May 2011

Received in revised form 4 August 2011

Accepted 8 August 2011

Available online 15 September 2011

Dedicated to the memory of Professor D.L. Trimm an esteemed colleague and valued friend.

Keywords:

Mesoporous silica

Sulfated zirconia

One-pot

Catalysis

ABSTRACT

A series of non-periodic mesoporous silicas impregnated with both framework and nanocrystalline sulfated zirconia was prepared by a sol–gel process using an ionic liquid as a template. The physico-chemical properties of the mesoporous sulfated zirconia materials are described. Analysis of the new silicas indicates isomorphous substitution of silicon with zirconium and reveals the presence of extremely small (<10 nm) polydispersed zirconia nanoparticles in the materials with zirconium loadings of 28–41 wt.%. The materials with higher zirconium loadings catalyse the Meerwin–Ponndorf–Verley reductions of aldehydes and ketones for substrates with hydrogen-bond basicities, $pK_{\text{HB}} > 1.10$. In order to explain the catalytic activity, analysis of the acid sites of the materials using pyridine as a probe molecule reveals that in all cases the majority are Brønsted acid sites, with only a small number of Lewis acid sites present in those materials with low zirconium loadings.

© 2011 Elsevier B.V. All rights reserved.

1. Introduction

The interest in sulfated zirconia in particular, and the sulfated metal oxides in general, stems in part from the observation that relatively mild sulfating procedures, followed by calcination, dramatically increase the surface area, surface acidity and the catalytic activity for reactions involving carbenium ion intermediates. ZrO_2 is an amphoteric oxide with a monoclinic structure at room temperature [1], which changes reversibly to tetragonal [2] and then cubic (distorted fluorite) modifications at higher temperatures. In contrast, the sulfation treatment cracks the sample into a high-surface area and strongly acidic tetragonal sulfated ZrO_2 material [3].

The structure of the sulfated surface remains the subject of conjecture. Bear and co-workers reported the structures of a series of zirconium sulfates in the late 1960s [4–11]. Typically, these solids contain ZrO_7 or ZrO_8 polyhedra, linked by SO_4^{2-} tetrahedra [12–14]. Sulfated zirconia has been suggested to contain surface layers of pyrosulfates or monosulfates, depending on the sulfur loading, as well as $(\text{ZrO})_3\text{S}=\text{O}$ groups, and the involvement of adjacent surface-bound water molecules with the sulfate species [15–17].

Perhaps paradoxically, although there is a considerable industrial need for green superacid catalysts, in particular to replace the chlorinated aluminium oxide and aluminium trichloride used in isomerisations, alkylations and hydrations, there are relatively few effective solid superacid catalysts [18,19]. Solid superacids, capable of operating as proton exchange membranes at elevated temperatures, are also desirable materials for incorporation in fuel cells [20].

However, in industrial practice, sulfated zirconia, although an effective solid acid catalyst, is not cheap, is subject to deactivation by coke formation, and catalysts can be difficult to regenerate [21,22]. The contrary drivers of promise and limitations, as well as the recognition that the properties of sulfated zirconia are highly dependent on the synthetic precursors and method [22], have inspired a large number of synthetic strategies directed at higher catalytic activities and greater chemical stability, frequently by increasing the surface area and/or maximizing the fraction of zirconium atoms available to reactants [23]. These attempts fall predominantly into eight main categories: additives (e.g., Pt, WO_3) can be doped or added to the sulfated zirconia, sulfated zirconia can be supported on high surface area oxides (mainly SiO_2), high surface area zirconia can be prepared and sulfated, the sulfated zirconia can be prepared as a mesoporous solid [24], or as nanoparticles, either unsupported or supported on high surface area oxides, or zirconium can be substituted into high surface area oxides (e.g., silicalite [25], APO-5 [26], MCM-41 [27–29], SBA-15 [30–35], MCM-48 and mesoporous oxides [36,37]) and molecular zirconium precursors [38]

* Corresponding author. Tel.: +61 293512581; fax: +61 293513329.

E-mail address: th.maschmeyer@chem.usyd.edu.au (T. Maschmeyer).

can be grafted onto suitable solids. Several microporous crystalline zirconium silicate zeolitic materials have been reported (e.g., MFI with $300 > \text{Si}:\text{Zr} > 50$) [39].

Porous ZrO_2 aerogels can be prepared with surface areas in the range $100\text{--}200\text{ m}^2/\text{g}$, but these materials readily sinter at temperatures in excess of 400°C , their surface areas decreasing as they transform to the monoclinic and metastable tetragonal phases [40]. The synthesis of mesoporous zirconia, which might then be sulfated, was attempted soon after the reports of mesoporous silica [41–45]. However, these materials were often amorphous and their pore structures were frequently unstable and collapsed in the absence of the structure-directing template [46]. Mesoporous zirconia can be stabilised by the presence of sulfate groups, but this material also frequently collapses when heated above 400°C [47]. ZrO_2 can also be deposited on the walls of mesoporous SBA-15 [48].

An alternative approach to mesoporous zirconia has been the replicate method, in which ZrO_2 is formed within the pores of the “hard template”, SBA-15, which is then removed by leaching with aqueous sodium hydroxide, leaving a crystalline, porous tetragonal ZrO_2 , in which the existence of Si-O-Zr crosslinks are suggested to stabilise the mesoporous structure of the crystalline material [49]. Ye et al. have recently reported the preparation of a mesoporous ZrO_2 with improved thermal stability (to 700°C) by heating the freshly prepared material in its mother liquor at $110\text{--}150^\circ\text{C}$ before calcination. Nevertheless, the BET surface areas of these mesoporous materials were only moderate ($85\text{--}269\text{ m}^2/\text{g}$) and their thermal stabilities, although an improvement, did not match those of silicon-based MCM-41, nor were they treated with sulfate [50]. Furthermore, nanocrystalline ZrO_2 with crystalline walls consisting mainly of tetragonal ZrO_2 and containing macro- and mesopores has been reported recently [51].

Alternatively, a triblock copolymer can be used to synthesise crystalline cubic ZrO_2 nanoparticles of about 7 nm diameter which self-assemble into a mesoporous structure [52]. This material can be sulfated and the Lewis acidity of the sulfated material demonstrated by its ability to catalyse the benzylation of mesitylene at 75°C . Other recent examples of nanostructured sulfated ZrO_2 are prepared by precipitation in the presence of structure directing agents such as hexadecyltrimethylammonium bromide, Pluronic 123 and Brij-56 [53]. These materials have been used as catalysts for the isomerisation of *n*-butane [54].

Recently, zirconium has been incorporated into the worm-like mesoporous material, TUD-1, giving stable catalytic materials with enhanced acidity [55,56]. Similarly, Zr can be incorporated into SBA-15 as both isolated Zr centres within the framework and (at higher Zr loadings) as small aggregates on the pore walls [57]. This material catalysed the pinacol rearrangement. Other examples have been reported in which Zr is incorporated in SBA-15 [35,58]. Similarly, $\text{ZrOCl}_2 \cdot 8\text{H}_2\text{O}$ and TEOS can be hydrolysed in the presence of NaCl and the triblock copolymer P123 to produce, after aging, calcination, impregnation with H_2SO_4 and recalcination, an ordered mesoporous silica, similar to SBA-15, with nominal Si/Zr ratios between 2 and 5 [59].

Mesoporous materials are often effective catalysts or catalyst supports. However, few catalytic reactions require that the pores be regularly ordered. Since, in the case of ZrO_2 -derived materials, regular pore ordering of mesoporous materials frequently leads to thermally unstable materials, and given the high costs of the templates used in these syntheses, a more general strategy in catalyst syntheses is to concentrate on the mesoporosity, rather than the pore ordering, of the catalytic materials.

On the basis of our recent demonstration that ionic liquids could be used to prepare high surface area silicas with a sponge-like, 3-dimensional topology [60], as well as to stabilise metal chalcogenide nanoparticles [61], we reasoned that ionic liquids might be suitable media for the single-pot preparation of thermally stable, high

surface area mesoporous supported sulfated zirconia either as supported nanocrystals or with silicon isomorphically substituted by zirconium. We were also encouraged by the report of the incorporation of Zr into TUD-1 [55,56,62], although these materials had not been sulfated. Recently, Natalie et al. have reported a novel synthetic method, based on the copolymerisation of methacrylate-functionalised silica monomers and zirconium tetramers, to form mixed oxide materials of ZrO_2 dispersed in an SiO_2 matrix [63]. The acid/base properties of materials with high and low zirconium contents (Zr/Si atomic ratios of 1:2.5 and 1:20, respectively) were investigated by infrared spectroscopy. They concluded that under appropriate heating conditions, the acidic properties of hydrogen-bonded pairs of silanol groups were modified by the presence of ZrO_2 , and that more acidic sites were present in samples with the higher zirconium content. It is of interest, therefore, to examine how these variations in acidity can be further modified by sulfating the zirconia and how the combination of higher zirconium loading and sulfating affects catalytic activity in a mesoporous material.

Our investigations into single-pot preparations of high surface area mesoporous SiO_2 support, impregnated with sulfated ZrO_2 , and the characterisation and catalytic behaviour of the new materials in the Meerwin–Ponndorf–Verley reductions of aldehydes and ketones, are described herein.

2. Experimental

2.1. Materials

Zirconyl chloride octahydrate, tetraethoxysilane (TEOS), tetraethylammonium hydroxide, hydrofluoric acid (48 wt.% in water), (all Sigma Aldrich), boric acid, hydrochloric acid (35%) (all Merck), and nitric acid (70%) (Univar) were all used without further purification. Silicon (1000 ppm) and zirconium (1000 ppm) standards for ICP analysis were obtained from Choice Analytical. 1-Hexadecyl-3-methyl-imidazolium bromide was prepared using a reported procedure [64].

2.2. Instrumentation

The nitrogen sorption isotherms at 77 K were measured using a Micromeritics ASAP2020 Surface Area and Porosity Analyzer. The data were obtained by liquid nitrogen adsorption and desorption at various nitrogen partial pressures and were analysed by the BJH (Barrett–Joyner–Halenda) and the BET (Brunauer–Emmett–Teller) methods. The pore size distribution curve was derived from the analysis of the adsorption branch of the isotherm.

Powder X-ray diffraction patterns were collected on a PANalytical X'Pert PRO X-ray diffractometer using $\text{Cu K}\alpha$ radiation and a PIXcel solid-state detector. Low angle diffraction patterns were recorded in a continuous mode over the range of $1\text{--}10^\circ 2\theta$ using a step size of $0.040^\circ 2\theta$ with a count time/step of 26 s. Wide angle diffraction patterns were recorded in the continuous scanning mode over the range $10\text{--}70^\circ 2\theta$ using a step size of $0.0131^\circ 2\theta$ with a count time/step of 300 s.

Metal and silicon concentrations were determined by ICP analyses, which were performed on a Varian Vista AX ICP-AES. The samples were prepared in the following manner. To a silica sample in a polyethylene bottle (20–30 mg, dried for 12 h at 100°C) were added concentrated HNO_3 (1 mL) and HF (2.5 mL, 48 wt.%) and this mixture was stirred at room temperature for 8 h. Then a saturated boric acid solution (20 mL) was added. The resulting solution was then diluted to 50 mL with deionised water.

Diffuse reflectance UV–Vis spectra were recorded using a Cary 5E UV–Vis–NIR spectrophotometer in diffuse reflectance mode using an integration sphere. Reflectance data were converted to absorbance using the Kubelka–Munk method (arbitrary units).

Visible Raman spectroscopy was performed using a Renishaw inVia Raman microscope fitted with a 25 mW 488 nm excitation source, 1800 l/mm grating, and measured using a 50× objective. Raman spectra were recorded using a Bruker MultiRAM Raman spectrometer with a Nd YAG laser at 1064 nm. Spectra were acquired using a laser power of 500–1000 mW and 500–5000 scans and were sample dependent. The spectra were measured using a liquid N₂ cooled Ge detector with a resolution of 4 cm⁻¹.

Infrared spectroscopy was performed using a Bruker IFS 66v infrared spectrometer equipped with a KBr beam splitter. Data were collected over a spectral range of 1000–375 cm⁻¹ using a Pike Miracle Single Bounce ATR accessory. The internal reflection element was a composite diamond KRS5 crystal. Spectra were recorded with co-addition of 32 scans at a spectral resolution of 4 cm⁻¹.

Transmission electron micrographs were recorded digitally with a Gatan slow-scan charge-coupled device (CCD) using a Phillips CM120 Biotwin electron microscope operating at 120 kV. The samples were prepared by dispersing the powder products as an ethanol slurry, which was then deposited and dried on a holey carbon film on a Cu grid.

High-resolution transmission electron microscopy (HRTEM) was performed using a JEOL 3000F microscope operating at 300 kV. Specimens for HRTEM studies were dispersed in ethanol, accumulated on a copper holey carbon grid and dried at room temperature. The specimens were additionally evaporated with carbon in order to prevent excessive charging and decomposition of the sample under the electron beam. During the microscope session the objective lens voltage was adjusted to sufficiently high underfocus values (~1000 nm).

X-ray photoelectron spectroscopy (XPS) measurements were made using a Specs spectrometer (Specs, Germany), equipped with Al X-ray source with monochromator operating at 200 W, a hemispherical analyser and a line delay detector with 9 channels. Survey spectra were acquired for binding energies in the range 50–1200 eV, using a pass energy of 30 eV. O 1s, Zr 3p_{3/2} and Si 2s region spectra were acquired at a pass energy of 23 eV with 10 scans to obtain higher spectral resolution (0.1 eV step) and lower the noise level. Spectra were analysed using CASA software.

Catalytic reactions were monitored with a Shimadzu GC-17A Gas Chromatograph (GC) fitted with an SGE capillary column (BPX5, 30 m × 0.25 mm × 0.25 μm) after including calibration with mesitylene as internal standard.

The nature of the acid sites was determined through the adsorption of pyridine onto the materials (dried at 110 °C for 24 h). This was achieved by placing the silicas in a desiccator (using P₂O₅ as the desiccant) with a vial of pyridine for 72 h at room temperature. After this time the vial of pyridine was removed and the desiccator was evacuated and filled with N₂. This process was repeated until no pyridine persisted. The samples were then analysed using a Linkam FTIR600 environmental cell purged with N₂ using a Bruker MultiRAM Raman spectrometer with a Nd YAG laser at 1064 nm (800 mW and 2000 scans).

2.3. Syntheses

Zirconium oxide was prepared by the addition of water to an ethanolic solution of zirconium butoxide such that the Zr:H₂O was 1:2. Immediately a white gel was formed. The sample was dried and calcined at 450 °C for 2 h. The surface area of this material was found to be 90.7 m²/g.

A typical synthesis of the mesoporous sulfated zirconia materials with various Si/Zr molar ratios was performed as follows: 1-hexadecyl-3-methylimidazolium bromide (0.8 g, 2.23 mmol) was dissolved in aqueous dilute HCl (25 mL, 2 M, 0.05 mol) and to this solution was added TEOS (1.7 g, 8.16 mmol). The mixture

was stirred at 40 °C for 4 h, and then the required amount of ZrOCl₂·8H₂O was added to the stirred mixture. The resulting mixture was then stirred at 40 °C for 20 h. The mixture was then transferred into an autoclave and heated at 100 °C for 2 days. The pH of the synthesis gel was adjusted to 7.5 by drop-wise addition of aqueous ammonia at room temperature. The resulting mixture was hydrothermally treated at 100 °C for another 2 days. The final solid was collected by filtration, washed with water until no chloride was detected in the washings, and dried at room temperature. The solids obtained were impregnated with aqueous H₂SO₄ (0.5 M 25 mL) at room temperature for 30 min. The sulfated samples were then filtered, dried at 100 °C and calcined at 550 °C in air for 10 h.

2.4. General procedure for the Meerwin–Ponndorf–Verley reductions

All reductions were performed under a nitrogen atmosphere at 80 °C. SZ-SiO₂ (8, 25 mg) was added to a 2-neck flask prior to the addition of 2-propanol (4 mL) and mesitylene (0.1 mL, internal standard) and the reaction mixture was heated to 80 °C. When the desired temperature was reached, the ketone or aldehyde (2 mmol) was added. The reaction was monitored by taking small samples (~0.1 mL). The samples were centrifuged to remove the catalyst and diluted with hexane prior to analysis by GC.

3. Results and discussion

The mesoporous silicas impregnated with sulfated zirconia (2–9) were prepared using a modification of the method described by Du and co-workers [59]. The method (schematically represented in Fig. 1) involved the hydrolysis of the silica precursor (TEOS) in dilute HCl in the presence of the template 1-hexadecyl-3-methylimidazolium bromide at 40 °C for 4 h after which time the required amount of ZrOCl₂·8H₂O was added to achieve the desired Si:Zr ratio. In addition, a purely siliceous material (1) was prepared using an identical process. This synthesis differs from that of Zr-TUD-1 in that it does not proceed through silatrane intermediates [65].

Zirconium oxychloride, used in these syntheses, is present as the tetranuclear species [Zr₄(OH)₈(H₂O)₁₆]⁸⁺ in the crystal [66] and in aqueous solution [67] at low pH. It has been shown that the more acidic the solution, the less polymerisation to higher molecular weight species occurs [68]. Hence, at pH ~1 used herein, the zirconium species can be expected to be predominately the tetramer. From the mechanistic point of view, it is likely that the synthesis of mesoporous sulfated zirconia using [C₁₆MIM]Br as the templating agent is mediated by the presence of Br⁻/Cl⁻ ions in the synthesis mixture as was observed by Wong et al. in the analogous CTAB templated system [32]. In such a case the synthesis was shown to proceed by a S⁺X⁻I⁺ pathway [32], in which S⁺ stands for the [C₁₆MIM] cation, X⁻ for Br⁻ anion and I⁺ for cationic zirconium species [69].

Nitrogen adsorption–desorption isotherms recorded at 77 K reveal classic Type IV curves which indicate the materials are mesoporous in nature (Fig. 2). These materials have pore sizes in the range of 2–50 nm, and the Type IV isotherms exhibiting hysteresis indicate that capillary condensation is occurring during the adsorption process. The surface area, pore volume and pore size data of mesoporous sulfated silica–zirconia samples are presented in Table 1. The BET surface area and pore volumes show the expected decreases with increasing zirconia content: the surface areas decrease from 482 to 343 m²/g and the pore volumes decrease from 1.34 to 0.43 cm³/g. The dramatic decrease in surface area with increasing Zr loading indicates that pore blocking may be occurring as ZrO₂ nanoparticles are deposited into the pores of the

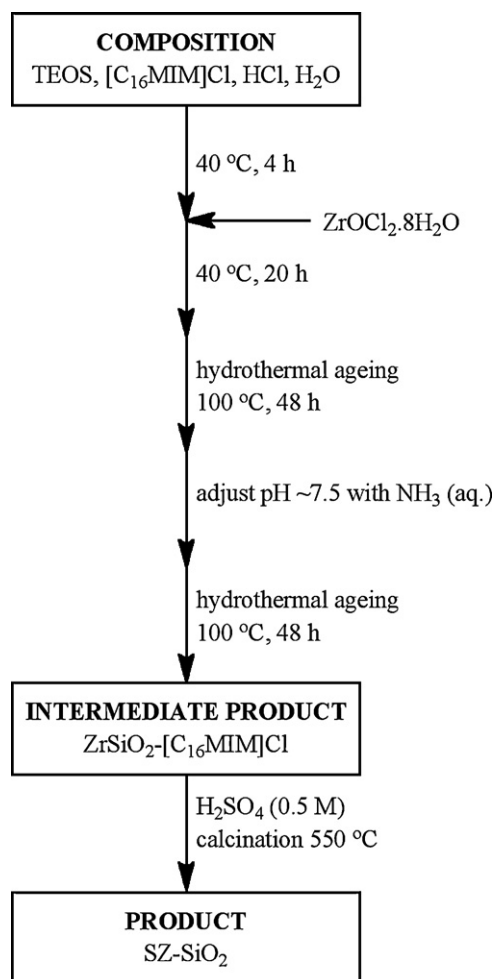


Fig. 1. Schematic representation of the syntheses of the SZ-SiO₂ materials.

materials. In addition to this, the very high Zr loadings in materials **6–9** may have resulted in a collapse of the pore structure thus giving rise to the observed decrease in the surface areas. The silica prepared without any zirconium added had a surface area of 709 m²/g and a pore volume of 0.82 cm³/g.

The ratio of zirconia to silica was measured using ICP-OES analysis. As can be seen from Table 1 there is a significant loss of the added zirconium as a result of the washing process. In the case of the SZ-SiO₂ materials with the lowest Zr loadings (i.e. **2–5**), only 31–49% of the added zirconium was incorporated into the final product. At the higher loadings, however, there is a significant increase in the incorporation of the zirconium: the silicas **6–9**

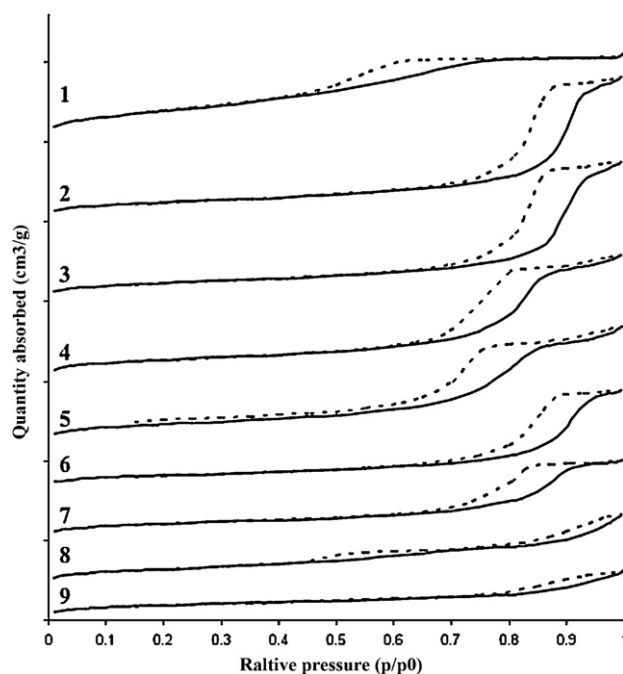


Fig. 2. Nitrogen adsorption (–)/desorption (···) isotherms for the materials **1–9** at 77 K.

have incorporation levels of between 61 and 69%. As a consequence, the zirconium loadings range from 1.0 to 41.4 wt.%.

Sulfur loadings were determined by elemental analysis of the materials prepared. As expected, the sulfur content of the materials increases with zirconium loading (Table 1). In the case of **5**, the sulfur loading is lower than expected and this may indicate the presence of larger ZrO₂ domains, compared to that of **4**, resulting in a lower available surface area for sulfate coordination. However, the amounts of sulfur are low for all materials, which indicates that the concentration of zirconium at the surface is low. Consistent with that interpretation, the surface sulfur densities range from 1 S atom/46 nm² (**2**) to 1 S atom/1 nm² (**9**), which can be compared with the estimated 4 sulfate groups for each nm² for a monolayer of sulfate groups on tetragonal sulfated ZrO₂ [70]. In the present work the highest sulfur loading is 1.69 wt.% for material **9** which has a zirconium loading of 61.5 wt.%. The sulfur loadings for the sulfated zirconia–silica materials prepared by Du and co-workers range from 2.0 to 3.9 wt.% for zirconium contents ranging from 20.1 to 33.8 wt.% [59].

The calcination temperature may explain the low sulfur loadings observed in these materials. It has been shown that for calcination temperatures greater than 480 °C there is a significant decrease in the sulfate concentration on pure zirconia samples [71,72] indicating that the coordinated sulfate is highly labile at elevated

Table 1
Physical properties of the prepared mesoporous sulfated zirconia–silica materials.

Sample	Added Zr (wt.%)	Zr loading ^a (wt.%)	Si/Zr (mol/mol)	Sulfur loading ^b (wt.%)	Zr/S	Surface area (m ² /g)	Pore volume (cm ³ /g)	Pore Size (Å)
1	–	–	∞	–	–	709	0.82	46
2	2.2	1.0	148	0.1	7.1	435	1.34	124
3	3.6	1.3	111	0.1	4.7	416	1.29	124
4	7.9	2.4	60	0.3	2.6	482	1.17	97
5	10.9	5.3	27	0.3	6.6	470	1.08	91
6	25.0	15.4	7.8	0.7	7.4	424	1.17	110
7	39.5	26.9	3.6	1.1	8.8	378	0.76	81
8	45.0	27.8	3.4	1.2	8.0	380	0.56	59
9	61.5	41.4	1.6	1.7	8.6	343	0.43	50

^a Determined by ICP-OES analysis.

^b Determined by elemental analysis.

Table 2

Relative concentrations of O, Zr and Si (%) at the surface of the SZ-SiO₂ materials as determined by ZPS.

Sample/absorption	O 1s	Zr 3p _{3/2}	Si 2s	Si/Zr
2	68.3	0.2	31.5	158
3	69.6	0.2	30.1	151
4	75.9	0.2	31.5	158
5	72.1	1.2	26.7	22
6	78.3	1.0	20.7	21
7	69.5	1.3	29.2	22
8	84.0	5.7	10.3	2
9	74.6	9.0	16.4	2

temperatures. In addition, the concentration of the H₂SO₄ solution that has been used to treat the zirconia has been found to have a marked effect on the final sulfate concentration in the final material: an increase in H₂SO₄ concentration from 0.02 M to 1.5 M sees a 7.2 times increase in sulfate concentration in the final materials [71]. Furthermore, recent work has shown that significant sulfate is lost when the calcinations are performed in a shallow bed, as the samples being investigated here prepared, compared to a calcination performed using a bed depth of a few centimetres [73]. As a consequence, it can be concluded that the low sulfate concentrations seen in the materials 2–9 are the result of two factors: the loss of coordinated sulfate during the calcination procedure and the low concentration of zirconia at the surface of the materials.

X-ray photoelectron spectroscopic (XPS) experiments were used to probe the surface composition of the SZ-SiO₂ materials. As can be seen in Table 2, the Zr surface concentrations for materials 2–7 are relatively low, indicating the bulk of the zirconia is located within the silica matrix. If nanoparticles were present on the surface of these materials Si/Zr ratios higher than those observed for the ICP would be expected: in the case of materials 2–7 the observed Si/Zr ratios are lower or correspond with the ICP data which indicates that there is no significant deposition of Zr at the surface; for materials 8–9 the Si/Zr ratio is significantly greater than that determined by ICP analysis indicating the presence of Zr at the surface of the material. The relative concentrations of zirconia increase considerably for silicas 8 and 9, suggesting the presence of ZrO₂ nanocrystallites on the surface of the silica (*vide infra*). Assuming that the silicon present within the samples is present as silica and setting the Si 2p binding energy at 103.6 eV (the value for SiO₂) [74], then the binding energy for Zr 3d_{5/2} has a corrected value of between 182.8 and 183.7 eV. These values are higher than for bulk ZrO₂ (182.2 eV) and closer to that of ZrSiO₄ and of Zr in Zr-TUD-1 (183.3 and 183.2 eV, respectively) [56,75]. Similarly, the O 1s values have a range of 531.7–532.3 eV, which are significantly higher than the binding energy seen in ZrO₂ but approximate those in Zr-TUD-1 and in SiO₂ (530.2, 532.4 and 532.9 eV, respectively) [56,75]. The values in Zr-TUD-1 were interpreted in terms of a larger number of Si–O–Si than Si–O–Zr bridges and most of the zirconium being in the framework, rather than present as domains of ZrO₂, consistent with a similar situation being present here [56]. Further confirmation of the incorporation of the Zr into the framework was obtained by IR and Raman studies of the materials (*vide infra*). The use of XPS to probe the S 2p binding energy was not possible in our study, due to the low sulfur loadings (as determined by elemental analysis), which resulted in the observed peaks having poor signal-to-noise.

The infrared spectra for the skeletal region of materials 1–9 are shown in Fig. 3. The spectra are similar to those of Zr-TUD-1, which were interpreted as consistent with most of the zirconium being present in the framework [56]. The spectra are dominated by absorptions assignable to the silica support: 460 cm^{−1} (O–Si–O bending), 800 cm^{−1} (Si–O–Si deformation), 1000–1100 cm^{−1} (Si–O stretch), ~1200 cm^{−1} (asymmetric Si–O–Si stretch), and 1625 cm^{−1} (molecular water bending). It should also be noted that the

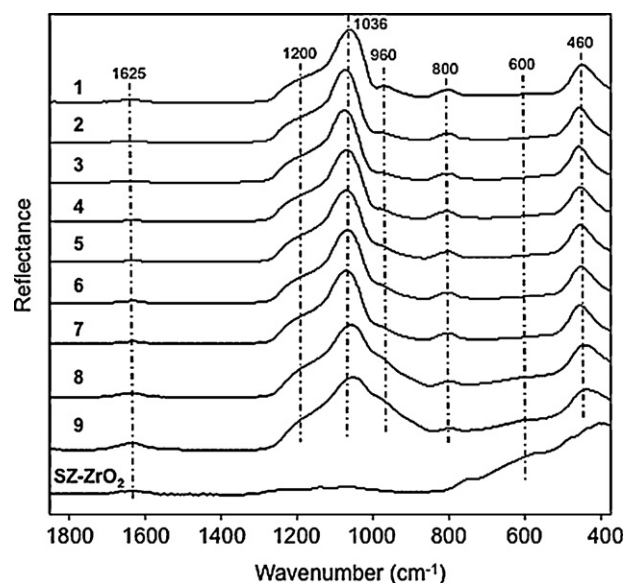


Fig. 3. Infrared spectra in the skeletal region of bulk sulfated zirconia (SZ-ZrO₂), silica (1) and the prepared SZ-SiO₂ samples 2–9.

absorptions assigned as silica framework stretches become considerably broader and less defined which is indicative of the incorporation of Zr into the silica framework through isomorphous substitution. Silica 1, in particular, shows a clear absorption at 960 cm^{−1} that is attributed to the Si–O stretch of silanol groups, and this absorption becomes broader and less well resolved with an increase in zirconium loading, which is indicative of the presence of Zr coordinated to the hydroxyls on the surface of these materials. An infrared absorption in zirconium-impregnated silicalite-1 at 965 cm^{−1} has been attributed to a Si–O–Zr asymmetric stretch [39]. The silicas with the highest Zr loadings, 8 and 9, show the appearance of a shoulder at ~920 cm^{−1}, which has previously been attributed to a Si–O–Zr stretch [76].

In addition, the spectra of 8 and 9 show a weak absorption at 600 cm^{−1} that corresponds to the presence of ZrO₂ in the materials (*cf.* the spectra of bulk ZrO₂ in Fig. 3). The absence of this weak absorption in silicas 2–7 indicates that the Zr has been incorporated into the silica framework by isomorphously replacing Si atoms. This observation is supported by TEM images of these materials (*vide infra*). The decreasing amount of silica with increasing zirconia loading is clearly visible in the intensity decrease of the absorption at 1000–1100 cm^{−1}. A similar trend is observed for the absorption at 460 cm^{−1}. The second derivative of the spectra (not shown) resolves a number of peaks under the absorption envelope for the peak at 1000–1100 cm^{−1} and clearly shows the influence of the zirconium in the silica framework: 1 has a maximum at 1036 cm^{−1} whereas materials 2–7 have maxima between 1053 and 1061 cm^{−1} while 8 and 9 have maxima at 1046 and 1034 cm^{−1}, respectively. A similar trend is observed for the absorption at 1200 cm^{−1}, which shifts to 1215 cm^{−1} as the Zr loading is increased. An absorption at 877 cm^{−1} observed in samples with high zirconium loadings, and assigned as a Zr=O stretch may also contribute to this envelope [39,77].

Attempts to record the visible Raman spectra of the prepared SZ-SiO₂ materials were unsuccessful due to the fluorescence of the samples at 488 nm. The Raman spectra were recorded using an excitation line of 1064 nm and are shown in Fig. 4. Broad unresolved features characterise the Raman spectra. The strongest feature occurs at 906 cm^{−1}, and based on the asymmetric peak shape, this absorption is clearly composed of a number of overlapping vibrations. For in the bulk sulfated ZrO₂ notable absorptions are observed

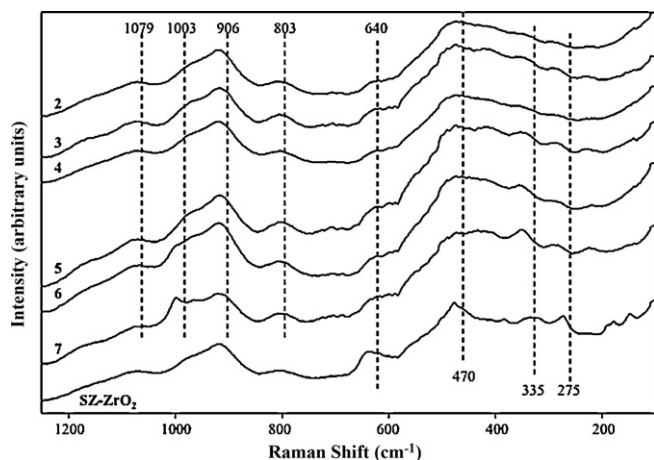


Fig. 4. Raman spectra (excitation: 1064 nm) of bulk sulfated ZrO_2 (SZ- ZrO_2) and the prepared SZ- SiO_2 samples 2–7.

at 640 and 478 cm^{-1} . The absorption at 640 cm^{-1} (in silicas 2–7) shifts to lower wavenumber as the zirconium loading decreases. The peak at 478 cm^{-1} is obscured in the silica samples by the intense absorption that results from O–Si–O bending. The absorptions at 275 and 335 cm^{-1} in the SZ- ZrO_2 sample can be seen at slightly higher wavenumber in the silica samples with decreasing intensity with lower zirconium loading. In the region 1200–800 cm^{-1} , the silicas display a series of overlapping absorptions at 1079, 1003, 906 and 801 cm^{-1} which are assigned to symmetric Si–O stretching modes. The positions are characteristic of tetrahedral units with three (Q_3), two (Q_2), one (Q_1) and zero (Q_0) bridging oxygen atoms, respectively [78]. Unfortunately, Raman spectra of 8 and 9 could not be obtained due to the large elastic scattering signal obtained from these samples. In such cases, several percent of the incident laser light can be scattered elastically into the spectrometer giving rise to a signal that is many orders of magnitude greater than that of the Raman scattering [79]. When the samples are weak Raman scatterers, as is the case with these samples, obtaining spectra is near impossible. The infrared and Raman spectra of $\text{ZrO}_2/\text{SiO}_2$ glasses contain an absorption at 975 cm^{-1} , (954 cm^{-1} , Raman) which is attributed to Zr–O–Si vibrations [80].

The diffuse reflectance UV–Vis spectra (not shown) of the SZ- SiO_2 materials 2–9 are effectively featureless and have no resemblance to pure zirconia (which exhibits a maximum at ~ 235 nm), indicating the absence of a bulk phase in the samples prepared. Bulk ZrO_2 has an absorption at ~ 235 nm [37] (monoclinic ZrO_2 absorbs at 240 and 310 nm [39]), whereas all SZ- SiO_2 materials have maxima that are below 200 nm, other than sample 9, which exhibits a weak maximum at ~ 205 nm. This single absorption is attributed to the O \rightarrow Zr ligand-to-metal charge transfer transition [37]. An electronic spectral absorption at 197 nm is attributed to an oxygen to metal charge transfer in isolated tetrahedral Zr(IV) ions in MCM-41 [29], and in Zr-TUD-1 [56], which is differentiated from the broad absorption at 227 nm (or 212 nm [39]) in ZrO_2 [48], assigned as an oxygen to Zr(IV) charge transfer.

The lack of a significant XRD reflection at low angle suggests little long range mesostructure in the material [81,82]. The diminution in peak intensity compared to the purely siliceous material 1 is attributable to the decrease in the pore size and the filling of the mesopores with the zirconium oxide nanoparticles at the highest loadings. The absence of additional reflections at low angle indicates that there is no ordering within the silica. The high angle ($2\theta > 10^\circ$) X-ray diffraction patterns of the mesoporous SZ- SiO_2 materials 2–9 (Fig. 5) reveal a broad reflection at $20\text{--}35^\circ 2\theta$ which is due to the amorphous nature of the silica support. In the case of 8 and 9, this reflection is significantly broadened compared to

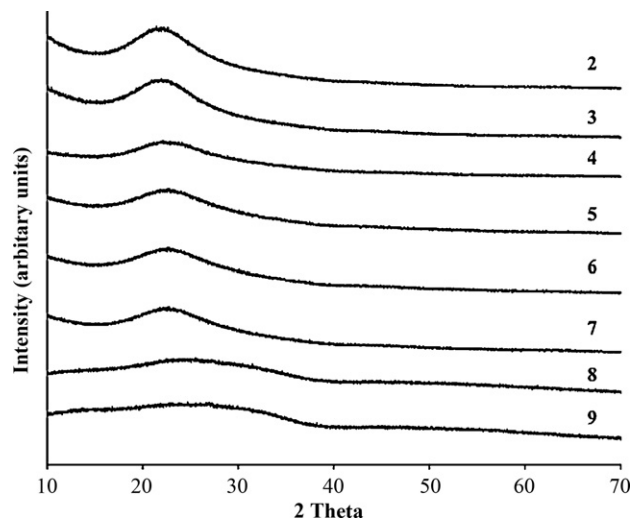


Fig. 5. High angle X-ray diffraction patterns of the prepared sulfated zirconia-silica samples 2–9.

that observed for materials 2–6 and this broadness may be due to the significant amounts of zirconium that have been incorporated into the silica framework. In all cases, there is no diffraction associated with a crystalline phase of ZrO_2 indicating no bulk crystalline zirconia is present.

The TEM images of the SZ- SiO_2 samples 3, 4 and 8 are shown in Fig. 6. As can be seen from these images, the silica does not possess long range order, which is consistent with our observations when using similar templates to produce high surface area mesoporous silica [60]. In addition, no large clusters of nanoparticulate zirconia are visible at the magnifications used, which indicates that the zirconia is present as either very small nanoparticles and/or is incorporated into the silica framework.

The dark field and HR-TEM images of several of the sulfated zirconia-silica samples are shown in Fig. 7. Dark field images show strong atomic number (Z) contrast, thus allowing heavier elements to be visualized. Hence, the dark field image of 7 (Fig. 7a) shows the dispersion of the Zr atoms within the silicon matrix and is representative of similar images obtained for materials 8 and 9 (not shown). In all the TEM images small crystalline particles associated with the walls of the silica surface are observable. In the case of silica 7 it was very difficult to observe the very small crystalline ZrO_2 particles in the HR-TEM but inspection of the electron diffraction pattern clearly indicates that polydispersed ZrO_2 particles are present. From the diffraction pattern it is evident that the material is poly-crystalline with some crystal orientation evident. The HR-TEM images of 8 and 9 clearly show the crystalline phase of ZrO_2 on the surface of the silica, with the particles being in the range 5–10 nm in size.

The catalytic activity of these materials was probed using the Meerwin–Ponndorf–Verley reductions [83] of aldehydes and ketones as a test reaction and SZ- SiO_2 (27.77 wt.% Zr (8) as a representative material, containing both nanoparticulate SZ- SiO_2 , and framework zirconium. This reaction, and its reverse, the Oppenheimer oxidation, has been catalysed by calcined hydrous zirconium oxide [84–87]. The results using SZ- SiO_2 (8) are collected in Table 3.

Sample SZ- SiO_2 (8) catalyses the Meerwin–Ponndorf–Verley reductions of a representative aldehyde (benzaldehyde) and a ketone (acetophenone). The conversions are comparable to those using Zr-TUD-1 as catalyst. The activity of the catalyst appears to correlate with the $\text{p}K_{\text{HB}}$ of the substrate [88], inasmuch as substrates with $\text{p}K_{\text{HB}} > 1.10$ are not converted. This effect and the substituent effects in arene substrates can be observed in the

Table 3Meerwin–Pondorff–Verley catalysed by SZ–SiO₂ (27.77 wt.% Zr, (**8**)).^a

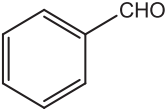
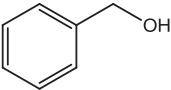
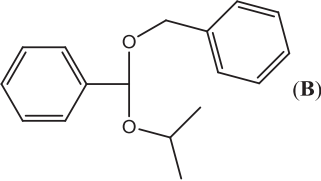
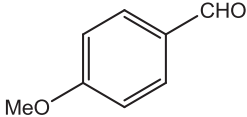
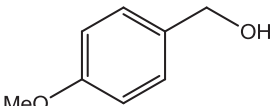
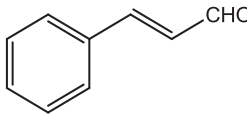
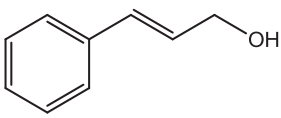
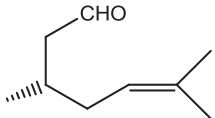
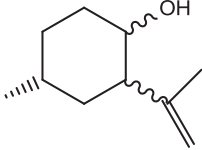

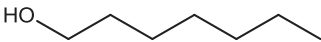
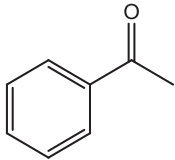
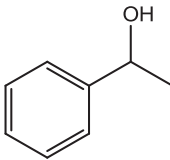
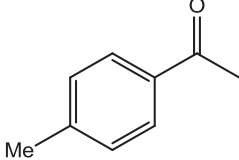
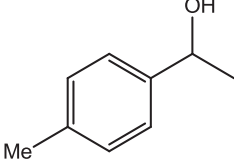
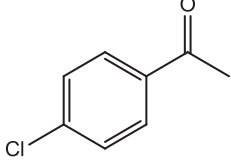
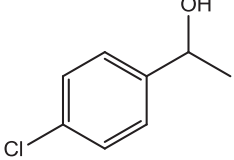
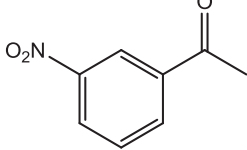
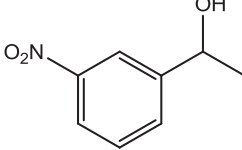
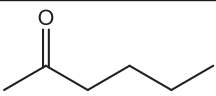
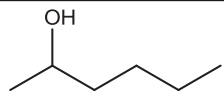
Substrate	Products	$pK_{\text{HB}}^{\text{b}}$	Conversion (%) ^c	Reaction time (h)
	 (A) +  (B)	0.78	48 (37% (A); 21% (B)) ^d	96
		1.10	9	96
		1.13	0	20
		N/A	6	96
		N/A	0 ^e	96
		1.11	12	48
		1.24	0	96
		0.93	8	96
		0.69	26	96

Table 3 (Continued)

Substrate	Products	pK_{HB}^b	Conversion (%) ^c	Reaction time (h)
		1.18	0	48

^a Reaction conditions: 25 mg catalyst, 4 mL 2-propanol, 2 mmol substrate, 100 μ L mesitylene (internal standard), 80 °C, performed under N₂ atmosphere.

^b Values of pK_{HB} obtained from Ref. [88].

^c The products were identified using GC–MS.

^d The formation of **B** results from the reaction of the generated alcohol and subsequent reaction with one equivalent of the starting aldehyde to form a hemiacetal and the resulting hemiacetal reacting with the solvent to form the observed acetal.

^e No products from the reduction of the aldehyde were seen, however, products resulting from the reaction of the aldehyde with the solvent (i.e. hemiacetal and acetal) were observed.

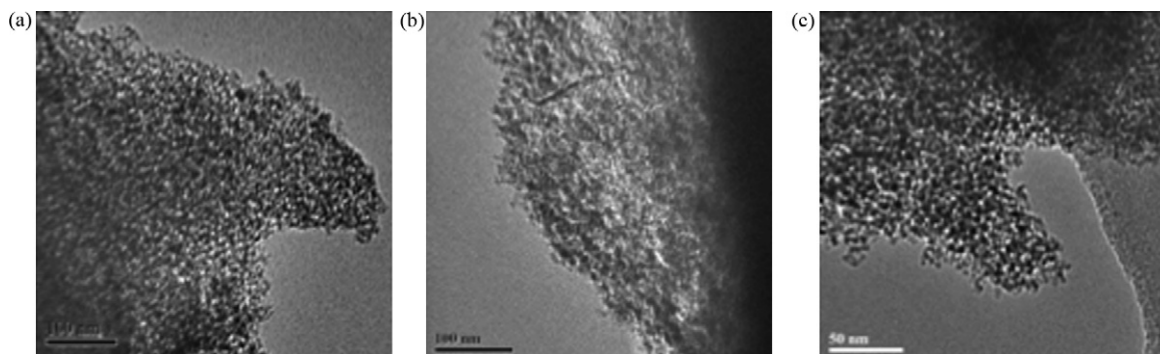


Fig. 6. Representative TEM images of the prepared SZ-SiO₂ samples: (a) silica **3** (1.34 wt.% Zr); (b) silica **4** (2.43 wt.% Zr); and, (c) silica **8** (27.77 wt.% Zr).

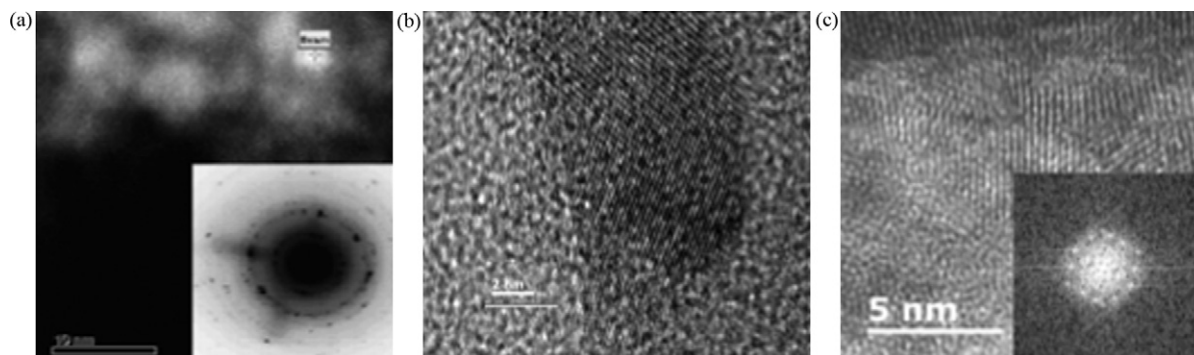


Fig. 7. HR-TEM images of the prepared SZ-SiO₂ samples **7–9**: (a) dark-field image of silica **7** (26.89 wt.% Zr); (b) silica **8** (27.77 wt.% Zr); (c) silica **9** (41.40 wt.% Zr).

results for the substituted phenylmethylketones, in which the *p*-Me derivative (pK_{HB} 1.24) is not converted, and the greatest conversion is observed for the *m*-NO₂ derivative. Although we observe no detectable reaction of cinnamaldehyde with 2-propanol over 20 h, this reaction is slow, even with ZrO₂ catalysts of “moderate activity” [89].

Given the low catalytic activities observed for the Meerwin–Ponndorf–Verley reductions, the nature of the acid sites on these materials was determined with FT-Raman spectroscopy using pyridine as a probe molecule. The most sensitive Raman vibration of pyridine is the symmetric ring breathing (ν_{CCN}) at 991 cm⁻¹. The interaction of pyridine with the acid sites of a support results in a shift of this Raman band to higher values, thus the position of the skeletal vibration band can be used to determine the nature of these acid sites. It has been determined that the interaction of pyridine with weak protonic sites through hydrogen bonding results in bands between 996 and 1008 cm⁻¹, or chemisorption at strong Brønsted sites results in bands between 1007 and 1015 cm⁻¹ or Lewis acid sites give rise to bands between 1018 and 1028 cm⁻¹ on solid surfaces [89–91]. As can be seen in Fig. 8, all the materials show a significant peak at 1007 cm⁻¹, which

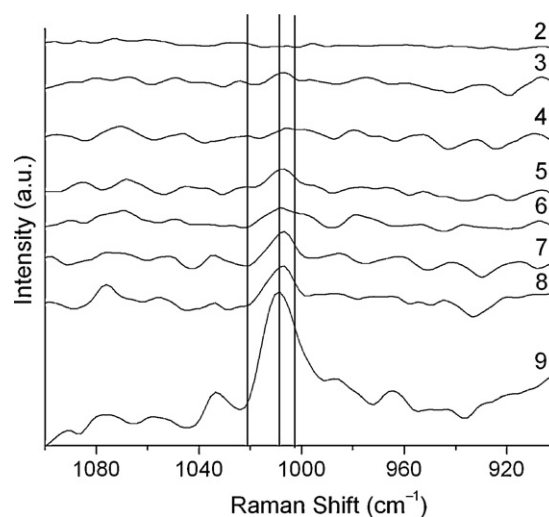


Fig. 8. Raman spectra of pyridine chemisorbed onto the SZ-SiO₂ materials **2–9** in the pyridine symmetric ring breathing vibration region.

increases in intensity with increasing zirconium content, that is attributable to strong Bronsted sites. In addition, the peak centred at $\sim 998\text{ cm}^{-1}$ reveals the presence of weak hydrogen bonded sites. Only materials 2–5 have Lewis acid sites that are indicated by the peak at $\sim 1024\text{ cm}^{-1}$. All of the materials do show some evidence of hydrogen bonding to the pyridine, as evidenced by the peak between 997 and 1002 cm^{-1} .

It is well established that the Meerwin–Ponndorf–Verley reduction is promoted by Lewis acid sites [83], however, more recent work has shown that Bronsted sites can also be active for the catalysis of this reaction [89]. Thus, the lack of Lewis acidic sites can explain the observed low catalytic activity. The lack of activity of the Bronsted sites is attributable to two factors: the first is that a high density of Bronsted sites has been observed to give lower catalytic activity for the Meerwin–Ponndorf–Verley reduction [89]; the second is that when zirconia materials are calcined at temperatures above 400°C a significant decrease in catalytic activity for the Meerwin–Ponndorf–Verley reduction results [87].

4. Conclusions

This study has shown that 1-hexadecyl-3-methylimidazolium bromide can be successfully used as the structure directing agent in a one pot synthesis of mesoporous sulfated zirconia. The mesoporosity is confirmed by the nitrogen absorption, XRD and electron microscopy measurements. The materials, prepared with varying ratios of zirconium to silica (up to $\sim 40\text{ wt.}\%$), displayed surface areas in the range $343\text{--}482\text{ m}^2/\text{g}$ and mesopore volumes ranging from 0.43 to $1.34\text{ cm}^3/\text{g}$. This method of preparation of the SZ-SiO₂ materials for loadings up to $41\text{ wt.}\%$ Zr results in the formation of nanocrystalline zirconia in the silica host, with the zirconium also present as polydispersed nanoparticles of ZrO₂ on the surface at the higher loadings. These conclusions are based on the lack of spectroscopic and X-ray diffraction evidence for large domains of ZrO₂ or sulfated ZrO₂, even at relatively high zirconium loadings. XPS revealed only small amounts of zirconium on the surface, consistent with the majority of the zirconium being incorporated in the SiO₂ framework. The materials display solid acid behaviour, active in the catalysis of the Meerwin–Ponndorf–Verley reductions of aldehydes and ketones with pK_{HB} values less than 1.1. Investigation of the nature of the acidic sites of the SZ-SiO₂ materials using pyridine as a probe molecule revealed predominantly Bronsted acid sites, which, when the materials are calcined above 400°C results in a considerable decrease in activity for the Meerwin–Ponndorf–Verley reduction.

Acknowledgements

Support from the Australian Research Council is gratefully acknowledged. L.C. gratefully acknowledges the receipt of a University of Sydney International Scholarship.

References

- [1] J.D. McCullough, K.N. Trueblood, *Acta Crystallogr.* 12 (1959) 507–511.
- [2] G. Teufer, *Acta Crystallogr.* 15 (1962) 1187.
- [3] M. Hino, K. Arata, *J. Chem. Soc. Chem. Commun.* (1980) 851–852.
- [4] I.J. Bear, *Aust. J. Chem.* 19 (1966) 357–361.
- [5] I.J. Bear, *Aust. J. Chem.* 20 (1967) 415–428.
- [6] I.J. Bear, *Aust. J. Chem.* 22 (1969) 875–889.
- [7] I.J. Bear, G.M. Lukaszewski, *Aust. J. Chem.* 19 (1966) 1973–1975.
- [8] I.J. Bear, W.G. Mumme, *J. Chem. Soc. Chem. Commun.* (1968) 609–611.
- [9] I.J. Bear, W.G. Mumme, *J. Chem. Soc. Chem. Commun.* (1969) 230–232.
- [10] I.J. Bear, W.G. Mumme, *Spectrochim. Acta A* 26 (1970) 755–760.
- [11] I.J. Bear, W.G. Mumme, *Rev. Pure Appl. Chem.* 21 (1971) 189–211.
- [12] Y.-L. Fu, Z.-W. Xu, J.-L. Ren, S.W. Ng, *Acta Crystallogr.* 61E (2005) m1520–m1522.
- [13] Z.-W. Xu, Y.-L. Fu, S.-Q. Teng, S.W. Ng, *Acta Crystallogr.* 62E (2006) m3420–m3422.
- [14] Z.-W. Xu, Y.-L. Fu, S.-Q. Teng, S.W. Ng, *Acta Crystallogr.* 63E (2006) m140–m142.
- [15] A. Hofmann, J. Sauer, *J. Phys. Chem. B* 108 (2004) 14652–14662.
- [16] M. Bensitel, O. Saur, J.-C. Lavalley, B.A. Morrow, *Mater. Chem. Phys.* 19 (1988) 147–156.
- [17] K. Arata, *Green Chem.* 11 (2009) 1719–1728.
- [18] V.V. Brei, *Teoreticheskaya i Eksperimental'naya Khimiya* 41 (2005) 165–175.
- [19] A. Corma, H. García, *Chem. Rev.* 103 (2003) 4307–4366.
- [20] W.H.J. Hogarth, J.C. Diniz da Costa, G.Q. Lu, *J. Power Sources* 142 (2005) 223–237.
- [21] G.D. Yadav, J.J. Nair, *Micropor. Mesopor. Mater.* 33 (1999) 1–48.
- [22] A. Corma, *Chem. Rev.* 95 (1995) 559–614.
- [23] S. Jaenicke, G.K. Chuah, V. Raju, Y.T. Nie, *Catal. Surv. Asia* 12 (2008) 153–169.
- [24] D.J. McIntosh, R.A. Kydd, *Micropor. Mesopor. Mater.* 37 (2000) 281–289.
- [25] M.K. Dongare, P. Singh, P.P. Moghe, P. Ratnasamy, *Zeolites* 11 (1991) 690–693.
- [26] M.K. Dongare, D.P. Sabde, R.A. Shaikh, K.R. Kamble, S.G. Hegde, *Catal. Today* 49 (1999) 267–276.
- [27] X.X. Wang, F. Lefebvre, J. Patarin, J.M. Basset, *Micropor. Mesopor. Mater.* 42 (2001) 269–276.
- [28] M.L. Ocelli, S. Biz, A. Auroux, *Appl. Catal. A* 183 (1999) 231–239.
- [29] L.F. Chen, J.A. Wang, L.E. Noreña, J. Aguilar, J. Navarrete, P. Salas, J.A. Montoya, P. Del Angel, *J. Solid State Chem.* 180 (2007) 2958–2972.
- [30] W. Hua, Y. Yue, Z. Gao, *J. Mol. Catal.* 170 (2001) 195–202.
- [31] F. Li, F. Yu, Y. Li, R. Li, K. Xie, *Micropor. Mesopor. Mater.* 101 (2007) 250–255.
- [32] M.S. Wong, H.C. Huang, J.Y. Ying, *Chem. Mater.* 14 (2002) 1961–1973.
- [33] J. El Haskouri, S. Cabrera, C. Guillem, J. Latorre, A. Beltran, D. Beltran, M.D. Maros, P. Amorós, *Chem. Mater.* 14 (2002) 5015–5022.
- [34] J.Y. Ying, C.P. Mehnert, M.S. Wong, *Angew. Chem. Int. Ed. Engl.* 38 (1999) 56–77.
- [35] B.L. Newkalkar, J. Olanrewaju, S. Komarneni, *J. Phys. Chem. B* 105 (2001) 8356–8360.
- [36] D.J. Jones, J. Jiménez-Jiménez, A. Jiménez-López, P. Maireles-Torres, P. Olivera-Pastor, E. Rodríguez-Castellón, J. Rozière, *J. Chem. Soc. Chem. Commun.* (1997) 431–432.
- [37] M.S. Morey, G.D. Stucky, S. Schwarz, M. Froba, *J. Phys. Chem. B* 103 (1999) 2037–2041.
- [38] X.-X. Wang, L. Veyre, F. Lefebvre, J. Patarin, J.-M. Basset, *Micropor. Mesopor. Mater.* 66 (2003) 169–179.
- [39] B. Raksh, V. Ramaswamy, S.G. Hegde, R. Vetrivel, A.V. Ramaswamy, *Catal. Lett.* 45 (1997) 41–50.
- [40] D.A. Ward, E.I. Ko, *Chem. Mater.* 5 (1993) 956–969.
- [41] J.A. Knowles, M.J. Hudson, *J. Chem. Soc. Chem. Commun.* (1995) 2083–2084.
- [42] M.J. Hudson, J.A. Knowles, *J. Mater. Chem.* 6 (1996) 89–95.
- [43] U. Ciesla, S. Schacht, G.D. Stucky, K.K. Unger, F. Schüth, *Angew. Chem. Int. Ed. Engl.* 35 (1996) 541–543.
- [44] P. Yang, D. Zhao, D.I. Margolese, B.F. Chmelka, G.D. Stucky, *Nature (London)* 396 (1998) 152–155.
- [45] J. Fan, S.W. Boettcher, G.D. Stucky, *Chem. Mater.* 18 (2006) 6391–6396.
- [46] M.S. Wong, J.Y. Ying, *Chem. Mater.* 10 (1998) 2067–2077.
- [47] A. Mondal, A. Zachariah, P. Nayak, B.B. Nayak, *J. Am. Ceram. Soc.* 93 (2009) 387–392.
- [48] C.K. Krishnan, T. Hayashi, M. Ogura, *Adv. Mater.* 20 (2008) 2131–2136.
- [49] B. Liu, R.T. Baker, *J. Mater. Chem.* 18 (2008) 5200–5207.
- [50] F. Ye, Z. Dong, H. Zhang, *Mater. Lett.* 64 (2010) 1441–1444.
- [51] H. Chen, J. Gu, J. Shi, Z. Liu, J. Gao, M. Ruan, D. Yan, *Adv. Mater.* 17 (2005) 2010–2014.
- [52] S.K. Das, M.K. Bhunia, A.K. Sinha, A. Bhaumik, *J. Phys. Chem. C* 113 (2009) 8918–8923.
- [53] M. Lutecki, O. Solcova, S. Werner, C. Breitkopf, *J. Sol-Gel Sci. Technol.* 53 (2010) 13–20.
- [54] M. Lutecki, C. Breitkopf, *Appl. Catal. A: Gen.* 352 (2009) 171–178.
- [55] A. Ramanathan, D. Klomp, J.A. Petersa, U. Hanefeld, *J. Mol. Catal. A* 260 (2006) 62–69.
- [56] A. Ramanathan, M.C.C. Villalobos, C. Kwakernaak, S. Telalovic, U. Hanefeld, *Chem. Eur. J.* 14 (2008) 961–972.
- [57] S.-Y. Chen, J.-F. Lee, S. Cheng, *J. Catal.* 270 (2010) 196–205.
- [58] S.-Y. Chen, L.-Y. Jang, S. Cheng, *Chem. Mater.* 16 (2004) 4174–4180.
- [59] Y. Du, Y. Sun, Y. Di, L. Zhao, S.H. Liu, F.-S. Xiao, *J. Porous Mater.* 13 (2006) 163–171.
- [60] A.A. Pujari, J.J. Chadbourne, A.J. Ward, L. Costanzo, A.F. Masters, T. Maschmeyer, *New J. Chem.* 33 (2009) 1997–2000.
- [61] T. Maschmeyer, M. Che, *Angew. Chem. Int. Ed.* 49 (2010) 1536–1539.
- [62] S. Telalović, J.F. Ng, R. Maheswari, A. Ramanathan, G.K. Chuah, U. Hanefeld, *Chem. Commun.* (2008) 4631–4633.
- [63] M.M. Natile, A. Galenda, A. Glisenti, S. Mascotto, S. Gross, *J. Non-Cryst. Solids* 355 (2009) 481–487.
- [64] C.J. Adams, A.E. Bradley, K.R. Seddon, *Aust. J. Chem.* 54 (2001) 679–681.
- [65] S. Telalović, A. Ramanathan, G. Mul, U. Hanefeld, *J. Mater. Chem.* 20 (2010) 642–658.
- [66] A. Clearfield, P.A. Vaughan, *Acta Crystallogr.* 9 (1956) 555–558.
- [67] C. Walther, J. Rothe, M. Fuss, S. Büchner, S. Koltsov, T. Bergmann, *Anal. Bioanal. Chem.* 388 (2007) 409–431.
- [68] A. Clearfield, G.P.D. Serrette, A.H. Khazi-Syed, *Catal. Today* 20 (1994) 295–312.
- [69] Q. Huo, D.I. Margolese, U. Ciesla, D.G. Demuth, P. Feng, T.E. Gier, P. Sieger, A. Fiorenzo, B.F. Chmelka, *Chem. Mater.* 6 (1994) 1176–1191.
- [70] C. Breitkopf, *ChemCatChem* 1 (2009) 259–269.
- [71] F.R. Chen, G. Coudurier, J.-F. Joly, J.C. Vedrine, *J. Catal.* 143 (1993) 616–626.
- [72] R.A. Comelli, C.R. Vera, J.M. Parera, *J. Catal.* 151 (1995) 96–101.
- [73] X. Li, K. Nagaoka, L.J. Simon, R. Olindo, J.A. Lercher, *Catal. Lett.* 113 (2007) 34–40.

- [74] L. Armelao, H. Bertagnolli, D. Bleiner, M. Groenewolt, S. Gross, V. Krishnan, C. Sada, U. Schubert, E. Tondello, A. Zattin, *Adv. Funct. Mater.* 17 (2007) 1671–1681.
- [75] A. Infantes-Molina, J. Mérida-Robles, P. Maireles-Torres, E. Finocchio, G. Busca, E. Rodríguez-Castillón, J.L.G. Fierro, A. Jiménez-López, *Micropor. Mesopor. Mater.* 75 (2004) 23–32.
- [76] Z. Dang, B.G. Anderson, Y. Amenomiya, B.A. Morrow, *J. Phys. Chem.* 99 (1995) 14437–14443.
- [77] K. Dehnicke, J. Weidlein, *Angew. Chem. Int. Ed. Engl.* 5 (1966) 1041.
- [78] M. Bouchard, D.C. Smith, C. Carabatos-Nédelec, *Spectrochim. Acta A* 68 (2007) 1101–1113.
- [79] R.L. McCreery, *Raman Spectroscopy for Chemical Analysis*, John Wiley and Sons, New York, 2000, p. 86.
- [80] S.W. Lee, R.A.S. Condrate, *J. Mater. Sci.* 23 (1988) 2951–2959.
- [81] Y.-Y. Huang, T.J. McCarthy, W.M.H. Sachtler, *Appl. Catal. A* 148 (1996) 135–154.
- [82] J.C. Jansen, Z. Shan, L. Marchese, W. Zhou, N.v.d. Puil, T. Maschmeyer, *Chem. Commun.* (2001) 713–714.
- [83] M. Boronat, A. Corma, M. Renz, *J. Phys. Chem. B* 110 (2006) 21168–21174.
- [84] M. Shibagaki, H. Kuno, K. Takahashi, H. Matsushita, *Bull. Chem. Soc. Jpn.* 61 (1988) 4153–4154.
- [85] M. Shibagaki, K. Takahashi, H. Kuno, H. Kawakami, H. Matsushita, *Chem. Lett.* 17 (1988) 1633–1636.
- [86] H. Kuno, K. Takahashi, M. Shibagaki, K. Shimazaki, H. Matsushita, *Bull. Chem. Soc. Jpn.* 63 (1990) 1943–1946.
- [87] S.H. Liu, S. Jaenicke, G.K. Chuah, *J. Catal.* 206 (2002) 321–330.
- [88] F. Besseau, M. Lucon, C. Laurence, M. Berthelot, *J. Chem. Soc. Perkin Trans. 2* (1998) 101–107.
- [89] F.J. Urbano, R. Romero, M.A. Aramendía, A. Marinas, J.M. Marinas, *J. Catal.* 268 (2009) 79–88.
- [90] A.A.M. Ali, M.I. Zaki, *Colloid Surf. A* 139 (1998) 81–89.
- [91] M.A. Aramendia, V. Borau, C. Jimenez, J.M. Marinas, J.R. Ruiz, F.J. Urbano, *J. Colloid Interface Sci.* 217 (1999) 186–193.